JACS
JOURNAL OF THE AMERICAN CHEMICAL SOCIETY
pubs.acs.org/JACS
Article

Zwitterionic Polymer Gradient Interphases for Reversible Zinc Electrochemistry in Aqueous Alkaline Electrolytes

Shuo Jin,[#] Peng-Yu Chen,[#] Yufeng Qiu, Zheyuan Zhang, Shifeng Hong, Yong Lak Joo,* Rong Yang,* and Lynden A. Archer*

Cite This: *J. Am. Chem. Soc.* 2022, 144, 19344−19352

Read Online

ACCESS | Metrics & More | Article Recommendations | Supporting Information

ABSTRACT: Aqueous alkaline zinc batteries are of scientific and technological interest because of the potential they offer for cost-effective and safe storage of electrical energy. Poor electrochemical reversibility and shape change of the Zn anode, propensity of Zn to become passivated by surface oxides and hydroxide films upon prolonged exposure to the electrolyte, and electroreduction of water are well-studied but remain unsolved challenges. Here, we create and study electrochemical and transport properties of precise, spatially tunable zwitterionic polymer interphases grown directly on Zn using an initiated-chemical vapor deposition polymerization methodology. In aqueous alkaline media, spatial gradients in composition—from the polymer−electrolyte interface to the solid−polymer interface—promote highly reversible redox reactions at high current density (20 mA cm^{-2}) and high areal capacity (10 mAh cm^{-2}). Via molecular dynamics and experimental analyses, we conclude that the interphases function by regulating the distribution and activity of interfacial water molecules, which simultaneously enables fast ion transport and suppression of surface passivation and the hydrogen evolution reaction. To illustrate the practical relevance of our findings, we study aqueous Zn||NiOOH and Zn||air batteries and observe that zwitterionic polymer interphases produce extended life at high currents and high areal capacity.

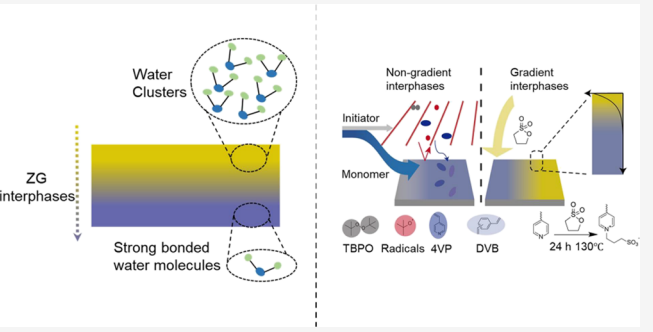

INTRODUCTION

Aqueous zinc (Zn) batteries have recently become the subject of intensive research efforts world-wide due to the expanding demand for safe, cost-effective, and long-duration storage to complement the rising supply of low-cost clean electricity from renewable resources.[1−3] Curiously, the vast majority of contemporary cell designs retain nearly all of the features of Volta's alkaline Zn−Cu battery pile invented and commercialized over two hundred years ago! Many of these cells are already available commercially (e.g., Zn||NiOOH, Zn||Air, Zn||MnO_2, etc.) and find use in cylindrical and coin-cell batteries used for remote controllers, in hearing aids, etc. It is known that a fundamental barrier to progress towards a truly low-cost technology for long duration storage in Zn batteries is the intrinsic chemical, morphological, and mechanical instability of the zinc anode in alkaline electrolytes. This leads to myriad anode failure modes: anode shape-change, premature short-circuiting, electronic disconnection and poor utilization of the active anode material, water breakdown and hydrogen evolution, to name a few. Consequently the short cycle life of commercial alkaline Zn batteries has become an accepted limitation of the technology, and despite the low cost and maturity of the chemistries at the anode and cathode, large-scale applications of such batteries are rare.[2,3]

It is understood that the instability of alkaline Zn systems results fundamentally from the incompatibility between Zn and aqueous alkaline electrolytes. This incompatibility manifests in a variety of challenges (e.g., Zn corrosion and formation of undesirable side products such as ZnO and $Zn(OH)_2$ that passivate the anode and limit utilization of the active material).[3] Heterogeneous interphases formed on Zn by these products cause additional problems, such as nonuniform, out-of-plane deposition, which upon battery recharge produces low-density porous structures,[4−6] and anode shape-change and orphaning[7−9] of the Zn electrode—all of which compromise cycle life of an electrochemical process. Thus, in spite of all of the advances made in Zn electrode and electrolyte designs over the past decade, it is difficult to achieve reversible-enough cycling of aqueous alkaline zinc batteries for the technology to live up to its promise.[10−13] We note further that, contrary to conventional wisdom, these effects are normally worse during low current density operation of the battery.[1] This underscores

Received: June 27, 2022
Published: September 16, 2022

https://doi.org/10.1021/jacs.2c06757
J. Am. Chem. Soc. 2022, 144, 19344−19352

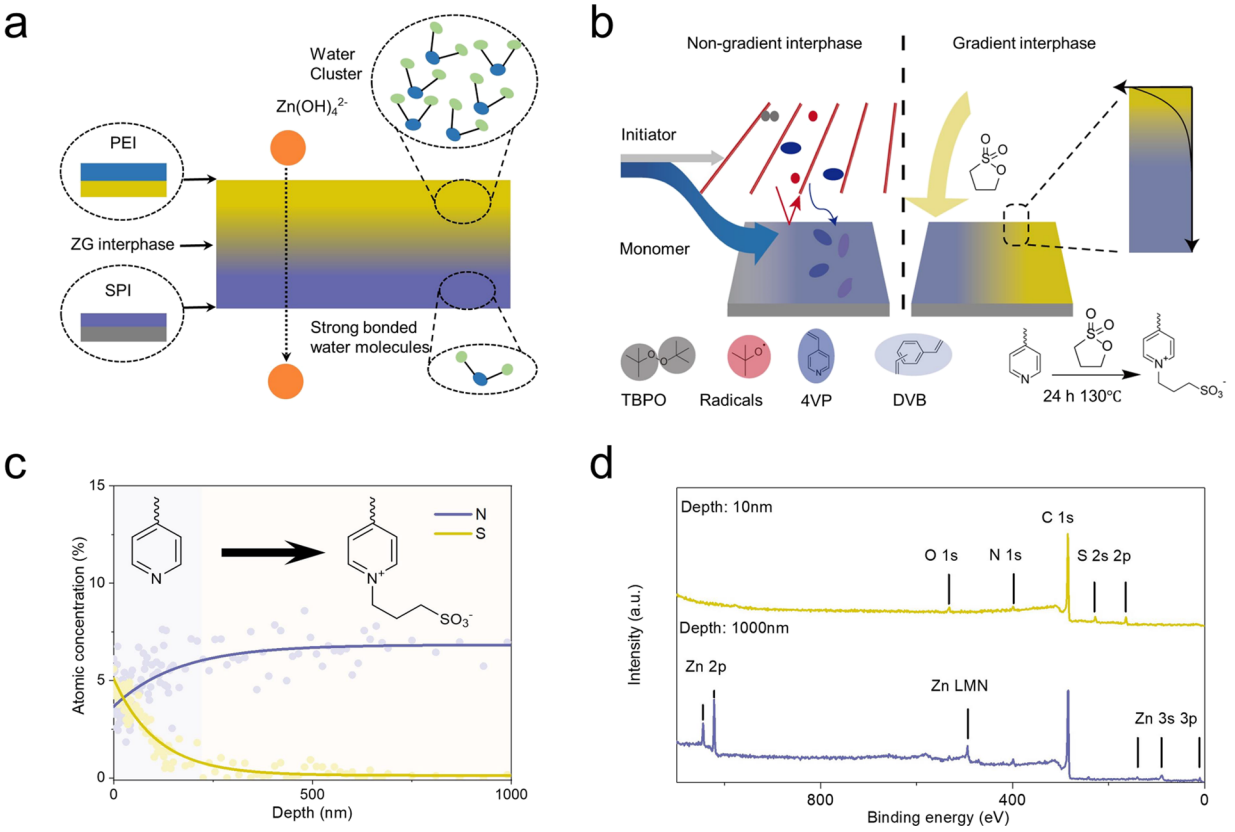

Figure 1. Design, synthesis, and characterization of ZG interphases. (a) Schematic illustrating the hypothetical effect of zwitterionic polymer gradient interphases on interfacial water. PEI indicates the polymer-electrolyte interphase. The flat navy-blue plate represents the aqueous electrolytes, and the flat yellow plate identifies the top layer of the ZG interphase. SPI represents the solid−polymer interphase. The flat blue plate represents the bottom layer of the ZG interphase, and the flat gray plate identifies the Zn plate. The color changes from yellow to blue indicates the gradient concentration of the zwitterionic polymer. The orange ellipse represents the solvated ion, and the black arrow indicates that the Zn^{2+} can diffuse through the ZG interphase. In the top layer, the water molecules are inclined to form clusters in the presence of the zwitterionic polymer, while in the bottom layer, a few water molecules are thought to be strongly bonded. (b) Schematic illustration of the synthesis of the gradient polymer interphases. Step 1: iCVD to form the precursor polymer films, p(4VP); step 2: vapor-phase derivatization. (c) The concentration gradient of sulfobetaine moieties along the surface normal direction evaluated by depth profiling of nitrogen and sulfur atomic concentrations using XPS survey scans. The inset shows the derivatization reaction achieved in the second step. (d) XPS survey scan of the zwitterion-gradient interphase at the etch depths of 10 and 1000 nm, respectively.

the importance of fundamental understanding and effective strategies for precisely regulating the underlying chemical and electrochemical processes required for achieving long cycle life operations.

The instability of the zinc anode in alkaline electrolytes, such as 6 M KOH + 0.2 M ZnO, stems in part from rampant chemical and electrochemical corrosion processes prevalent in these electrolytes.[10,11] Chemical corrosion is known to originate from the intrinsic amphoteric nature of Zn metal and is usually accompanied by a spontaneous hydrogen evolution reaction (HER). Once the Zn electrode comes into contact with an aqueous alkaline electrolyte (Figure 1a), $[Zn(OH)_4]^{2-}$ is generated, which decomposes to form ZnO, when the interfacial concentration of $[Zn(OH)_4]^{2-}$ exceeds a critical temperature-dependent value.[14,15] The electrochemical corrosion process originates fundamentally from the closeness of the reduction potential of $[Zn(OH)_4]^{2-}$ (−1.23 V vs SHE) and water (−0.829 V vs SHE). The electrodeposition of Zn metal as a result drives electrochemical HER[16] in alkaline electrolytes, further increasing the surface concentration of interfacial $[Zn(OH)_4]^{2-}$ and increasing the internal resistance of the battery cell. Both processes also contribute to the accumulation of harmful side-products, e.g., ZnO, at the electrolyte-anode interface, compromising the cycling performance of the Zn anode for a variety of reasons. The most important are the following: (1) the nonconductive ZnO layer slows interfacial ion transport and increases the interfacial impedance after cycling.[17,18] (2) The coarse ZnO layer is heterogeneous which has a negative influence on the reversible electrodeposition morphology. Specifically, it results in the fast growth of Zn at some places and limited growth at others. This leads to formation of a nonuniform mossy low density film that may easily grow along the electrode surface normal to either break away from the current collector (i.e., orphaned Zn) or to fill the interelectrode space, short-circuiting the battery.[19,20] Hence, suppressing the formation of ZnO layers is considered a key first step toward design of reversible Zn anodes in alkaline electrolytes. An essential second step concerns the electroreduction and loss of water from the cells. Specifically, at a typical Zn anode, free water molecules participate in both chemical and electrochemical HER process. This means that the interfacial water distribution and activity may be used to directly regulate the HER process (Figure S1). We hypothesize that an interphase design that limits access of free water to the Zn electrode surface but does not otherwise retard transport of

https://doi.org/10.1021/jacs.2c06757
J. Am. Chem. Soc. 2022, 144, 19344−19352

Zn ions to the electrode would dramatically improve the reversibility of Zn electrodes in aqueous alkaline electrolytes.

To evaluate this hypothesis, we constructed interphases on Zn using zwitterionic polymer films that can be derivatized in a manner that allows precise control of the water affinity along the surface normal (Figure 1a). Initiated chemical vapor deposition (iCVD) provides a facile strategy that enables precise, nanometer-resolved control of zwitterionic polymer properties normal to an interface by balancing diffusion kinetics with interfacial reaction kinetics.[21,22] In particular, through a two-step gas reaction process, we created nanosized zwitterionic polymer gradient interphases (ZG interphases) directly on a Zn foil surface (ZG@Zn). On the top layer of the interphase, a high concentration of zwitterionic groups is intentionally created to drive the free water to form clusters with high mobility (Figure 1a) via the field effect. The water clusters provide a water-saturated environment that facilitates ion movement.[23] Approaching the solid−polymer interface (SPI), the polymer coating is designed to transition to a pyridine-rich composition as the concentration of the zwitterionic moiety decreases. While the zwitterionic moiety interacts with water through induced dipoles, pyridine binds to water via strong hydrogen bonding (HB) interactions.[24,25] As such, the compositional gradient in the polymer coating translates to a free energy gradient that biases the distribution of free water molecules toward the polymer−electrolyte interphase (PEI), due to stronger hydration by the zwitterionic group than that of pyridine (Figure 1a). Furthermore, water molecules at the SPI are likely tightly bonded by the pyridine groups, increasing the energy barrier for water to participate in the chemical and electrochemical transformation at the SPI.[19,26,27] This is hypothesized to protect the Zn surface in alkaline electrolyte media. Therefore, using the nanoscale ZG interphase, the interfacial water distribution and activity can be controlled to suppress the HER, without adding substantial mass to the electrode.

Here, we focus on zwitterionic polymer interphases with thickness below 1000 nm in the present study—the precision synthesis of which falls well within the capabilities of current iCVD polymerization technology. Such interphases are of great interest for at least two additional reasons: (1) they allow one to easily probe the effects of interphase properties in interfacial processes, with minor influence from the bulk electrolyte; (2) they enable a comprehensive assessment of the working mechanisms of the polymer interphase by allowing in-depth study using a combination of experimental and molecular dynamics calculations. Furthermore, the chemical gradient can be controlled precisely by tuning the conditions of the diffusion-limited derivatizing reaction. This means that the synthesis approach can be easily expanded to create other gradient interphases for use in cases not considered in the present work. Here, we focus instead on the opportunities gradient interphases provide for exploring how the different properties (such as ion transport, electrochemical reactions, etc.) of the PEI and the SPI (Figure 1a) influence electrode reversibility.

RESULTS AND DISCUSSION

Designing Gradient Interphases on Zn Using iCVD. As illustrated in Figure 1b, a nongradient (NG) interphase, zwitterion-gradient (ZG) interphase, and completely zwitterion (CZ) interphase were synthesized by a two-step method that is reported in our previous work.[21,28] In the first synthesis step, a well-defined poly(4-vinylpyridine-*co*-divinylbenzene) (p4VP) film was fabricated using the iCVD technology with a controlled thickness at the nanometer level. Specifically, 4 sccm of 4-vinylpyridine (4VP), 0.15 sccm of divinylbenzene (DVB), and 0.6 sccm of initiator (*tert*-butylperoxide, TBPO) were introduced into a vacuum chamber (0.5 Torr) in which electrodes were placed on a cooled stage (25 °C). The cooled stage facilitated the physisorption of monomers that follows the Brunauer−Emmett−Teller isotherm. The free-radical polymerization of the adsorbed monomers was initiated by surface impingement of radicals that were generated by homolytic cleavage of TBPO flowing through a hot filament array (230 °C). As a result, a polymer film with approximately 80% vinyl pyridine and 20% DVB crosslinkers was synthesized as an NG interphase. The choice of precursors is the result of balancing the functional group density and mechanical properties.[21,29] Molecular structures of the NG interphase were confirmed using Fourier transform infrared spectroscopy (FTIR) (Figure S2) where the peaks at 1415 and 1597 cm^{-1} were attributed to C═N stretching on the pyridine. The NG interphase deposited on a freshly polished Zn plate exhibits a water contact angle of 65 ± 0.8° (Figure S3).

In the second step, the copolymer film was treated by 25 Torr of 1,3-propanesultone vapor for 24 h under 130 °C to convert pyridine into pyridinium-based sulfobetaine p(4-VPPS) (Figure 1b). After derivatization, two characteristic absorbance peaks appeared at 1037 and 1350 cm^{-1} that are attributed to the symmetric stretching of the SO_3^- and SO_2 moieties (Figure S2), indicating a successful conversion of pyridine into sulfobetaine moieties.[30] The p(4-VPPS) film presented a super hydrophilicity with a contact angle of 6.3 ± 0.3° (Figure S3).

Notably, the diffusion-limited derivatization strategy spontaneously creates a concentration gradient from the PEI to SPI (Figure 1a,b). The penetration depth, defined as the depth where the conversion of pyridine drops to 37% ($1/e$), is affected by the degree of crosslinking, temperature, derivatization duration, and partial pressure of propanesultone. If the coating thickness is smaller than penetration depth, sulfobetaine moieties dominate the hydrophilicity of the film, resulting in a highly hydrated polymer coating. In contrast, if the coating thickness is greater than the penetration depth, the polymer coating exhibits a concentration gradient from p(4-VPPS) to p(4VP) decaying approximately exponentially.[28]

To characterize the penetration depth, an 800 nm p(4VP) was deposited on a freshly polished Zn plate followed by the derivatization. X-ray photoelectron spectroscopy (XPS) was performed to capture the nanometer-scale depth profiling. As shown by Figure 1c,d, the sulfur content (from the SO_3^- group) at the topmost surface was 5.59%, close to a theoretical content of 5.3%, indicating complete conversion of pyridine into sulfobetaine moieties. The sulfur contents decayed exponentially as we probed deeper into the derivatized film. At a depth of 117 nm, it decreased to 2.0%, corresponding to a conversion of 37%, and at 520 nm, it decreased to 0.05%, corresponding to a conversion of 1%. At a depth of 1000 nm, Zn signals appeared, implying that the film was etched through. The nitrogen signal from Figure 1c increased in concert with sulfur signal. Based on the depth profiling, the penetration depth, established by the balance of reaction and diffusion, was determined to be 117 nm, and film depth greater than 520 nm was assumed to be free of zwitterionic moieties. Thus, films thinner than 100 nm were completely converted as a CZ

https://doi.org/10.1021/jacs.2c06757
J. Am. Chem. Soc. 2022, 144, 19344−19352

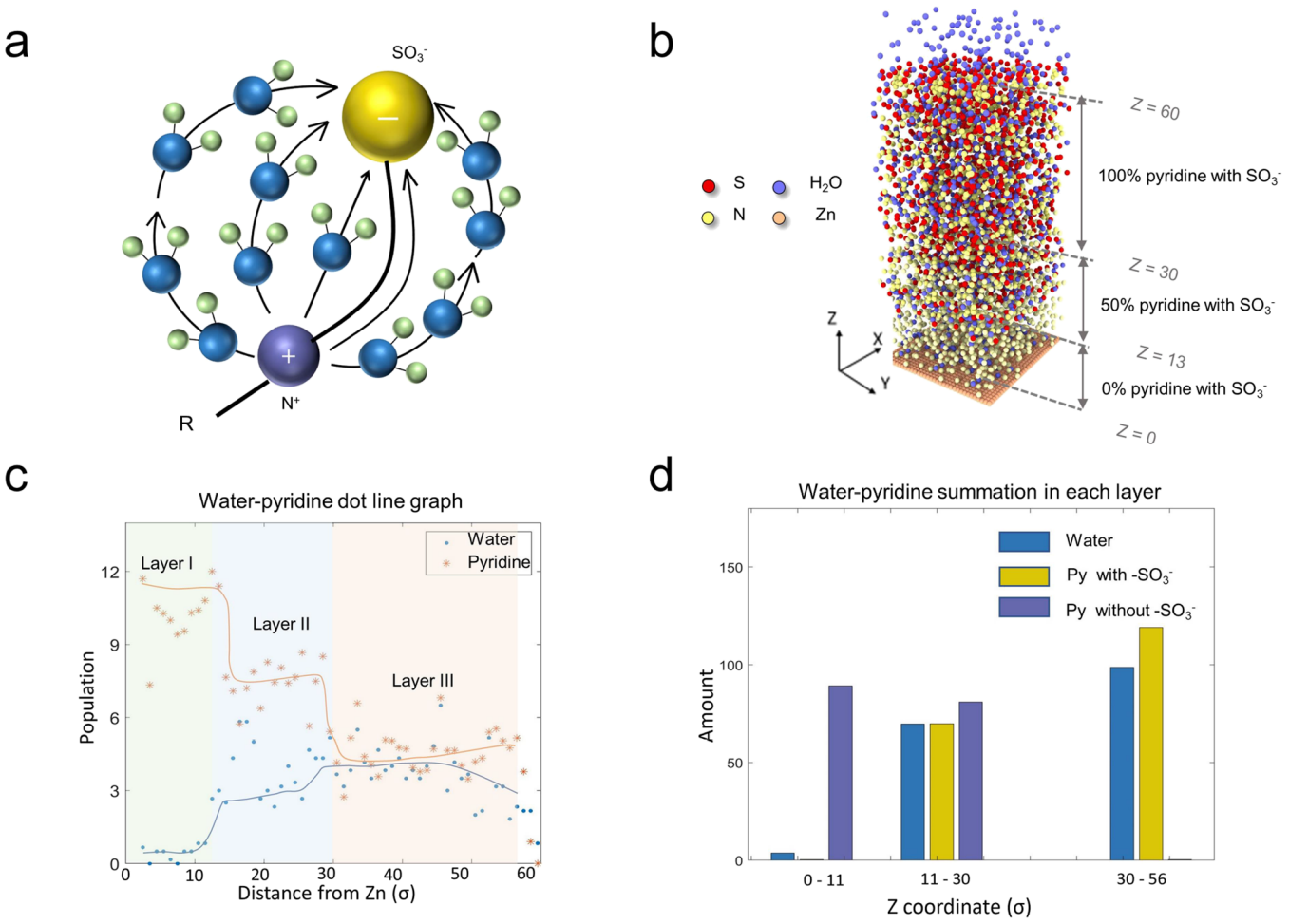

Figure 2. Water distribution in ZG interphases based on molecular dynamics simulation. (a) Hypothetical field effects between zwitterionic groups and free water molecules. Adapted with permission from ref 31, Copyright 2020 America Chemical Society. (b) Snapshot of MD simulation results for water distribution at a three-tiered layered zwitterionic polymer interphase on Zn, with different compositions of SO_3^- groups along the surface normal, where the concentration gradient of water molecule resembles that of the sulfobetaine p(4-VPPS). (c) Water and pyridine without $-SO_3^-$ distribution in different layers along the surface normal to the Zn substrate. (d) Cumulative amounts of water and pyridine (with and without $-SO_3^-$) at each layer extracted from (c).

interphase upon the derivatization described above; and ones thicker than 1000 nm were considered to have a sulfobetaine concentration gradient and labeled as the NG interphase.

Mechanism and HER Suppression. The mechanism and electrochemical and corrosion-resistance features of the NG, ZG, and CZ interphases were explored in the 6 M KOH, 0.2 M ZnO electrolyte. Two different modes of water−polymer interactions were investigated through these designed interphases: HBs of pyridine groups[24,25] and field-effect of zwitterionic groups,[27,31] as discussed above. Because of the tightly bound water molecules at the SPI of the pyridine-rich NG interphase, a high interfacial resistance of 254 ± 10 Ω was observed, 32 times larger than that of blank Zn foil (8 ± 5 Ω), reflecting the unfavorable ion migration and de-solvation kinetics (Figure S4), which can be further proved by the much lower exchange current densities (0.15 mA cm^{-2}) compared with the blank Zn foil (1.7 mA cm^{-2}) (Figure S5). Such a high interfacial resistance results in a much higher overpotential than blank, which leads to an unexpected low energy efficiency for aqueous batteries. In contrast, the zwitterionic groups allow the formation of water clusters (Figure 2a),[26,27,31] which, unlike the HBs between pyridine and water, enabled greater ion mobility.[30] Moreover, compared to the bound water in the NG films, the water clusters in the zwitterionic films, e.g., in the CZ interphase, led to stronger hydration and rapid ion transportation, albeit rapid HER kinetics at the SPI that resulted in more rampant corrosion (Figure S6). An ideal interphase should simultaneously enhance interfacial ion transportation and suppress HER, as demonstrated by the ZG interphase. Due to the high concentration of the zwitterionic moiety at the topmost surface, water clusters preferentially formed at the PEI,[26,27,31] whereas at the SPI, pyridine groups dominate, which lowered the propensity for water molecules to participate in HER.

To understand the underlying mechanism of the gradient structure, a ZG interphase model was constructed by molecular dynamics (MD) simulation. To be consistent with the different concentrations of the SO_3^- group (zwitterionic group), we set three layers with different ratios of SO_3^- groups from the top to the bottom. In the top layer, all p(4-VP) were converted to p(4-VPPS). In the middle layer, 50% of the poly(4-VP) was converted to p(4-VPPS) and only p(4VP) was present in the bottom layer. Through this model, we can estimate the water distribution in different layers and understand the effect of the ZG interphase on the distribution of interfacial water. Figures 2b and S7 show that the model is consistent with our XPS

https://doi.org/10.1021/jacs.2c06757
J. Am. Chem. Soc. 2022, 144, 19344−19352

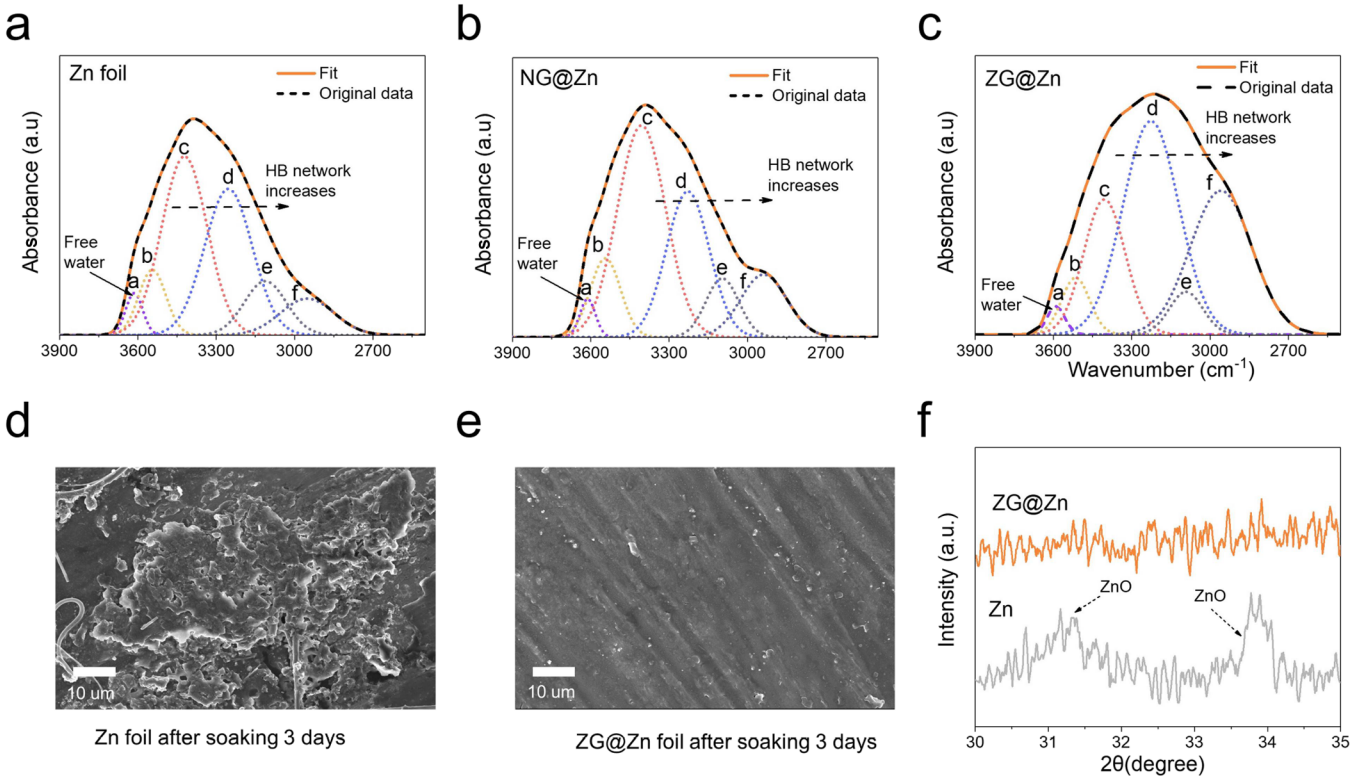

Figure 3. Proposed mechanism for regulating the interfacial water distribution and activity at ZG interphases. Peak fitting of the FTIR band associated with OH vibration of water molecules (a) at uncoated Zn, (b) at Zn with an NG interphase, and (c) with a ZG interphase. Peaks a–f indicate the hydrogen bond cooperativity: Peak a indicates free water molecules; as the peaks shift to the right, the HB network increases. (d,e) Morphology of Zn and ZG@Zn foil after soaking in 6 M KOH solution for 3 days. (f) XRD analysis of Zn foil and ZG@Zn foil after 3 days of soaking in 6 M KOH solution.

results since the distribution of all atoms is uniform. Figure 2c,d shows that the water concentration decreases from the top to the bottom, in which the top layer shows a high water concentration that results from the field effect of the zwitterionic group, while a few water molecules are observed in the bottom layer. Moreover, the concentration gradient of water matches that of the zwitterionic group (SO_3^-) (Figure 2d). Thus, the water distribution trend from the MD model proves that the free water molecules are inclined to form water clusters at the PEI, while the access of free water to the SPI is limited.

FTIR was used to analyze the microenvironment of water molecules at the uncoated zinc surface and all designed interphases by analyzing the vibration mode of the hydroxyl group in water. As Figures 3a–c and S8a show, the peaks a to f are assigned to the different levels of hydrogen bond cooperativity: a, free; b, 0 and 1; c, 2; d, 3; e, 3′; f, 4, where hydrogen bond cooperativity represents the number of water molecules in a water cluster or network.[32−34] Previous theoretical research[21] indicated that the cooperative enhancement led to more water molecules in a water cluster or network. Compared with an uncoated zinc foil surface, the NG interphase increased the intensity of peak f, indicating that the largest number of HBs increases from 8 to 12% (Figure 3a,b) and thus proving the tightly bound water molecules due to the pyridine moiety. In the CZ interphase (Figure S8a,b), peak f decreased from 8 to 6%, while peak d increased from 25 to 45% and peak e increased from 10.9 to 16.9%, indicating a strengthened field-effect-enabled water bonding mode of the zwitterionic groups[27,31] and weakened HBs.[24,25] The ZG interphase shows the combined characteristics of NG and CZ interphases. Compared with an uncoated zinc foil surface and other interphases (NG and CZ interphases), the intensity of peak d and peak f increased significantly, which accounts for 39% (peak d) and 30% (peak f) of all hydroxyl groups, respectively (Figure S8b). This result pointed to the increased number of water molecules in water clusters resulting from the field effect of the zwitterionic groups[26,27,31] and to the increased number of bound water molecules as a result of the strong HBs by the pyridine groups. Combining FTIR and MD, we demonstrated that the ZG interphase was capable of regulating the interfacial water distribution and water activity, resulting in a favorable interfacial water environment for ion transportation and corrosion resistance.

To evaluate the resistance performance of chemical corrosion of the ZG interphase, X-ray diffraction (XRD) and scanning electron microscopy (SEM) were performed. The enhanced chemical corrosion resistance was demonstrated by the morphologies of the Zn and ZG@Zn surfaces after immersion in 6 M KOH electrolyte for 3 days. As shown in Figure 3d,e, a coarse morphology was observed at the uncoated Zn surface that stemmed from chemical corrosion accompanied with side product accumulation. In contrast, the ZG@Zn surface showed an intact and smooth surface morphology after 3 days in 6 M KOH electrolyte. XRD spectra of uncoated Zn foil and ZG@Zn surfaces further proved the protection from the ZG interphase, where no ZnO peaks at the ZG@Zn surface were detected (Figure 3f).

For electrochemical corrosion, the ZG interphase demonstrated a decreased HER (Figure 4a), which was attributed to

https://doi.org/10.1021/jacs.2c06757
J. Am. Chem. Soc. 2022, 144, 19344−19352

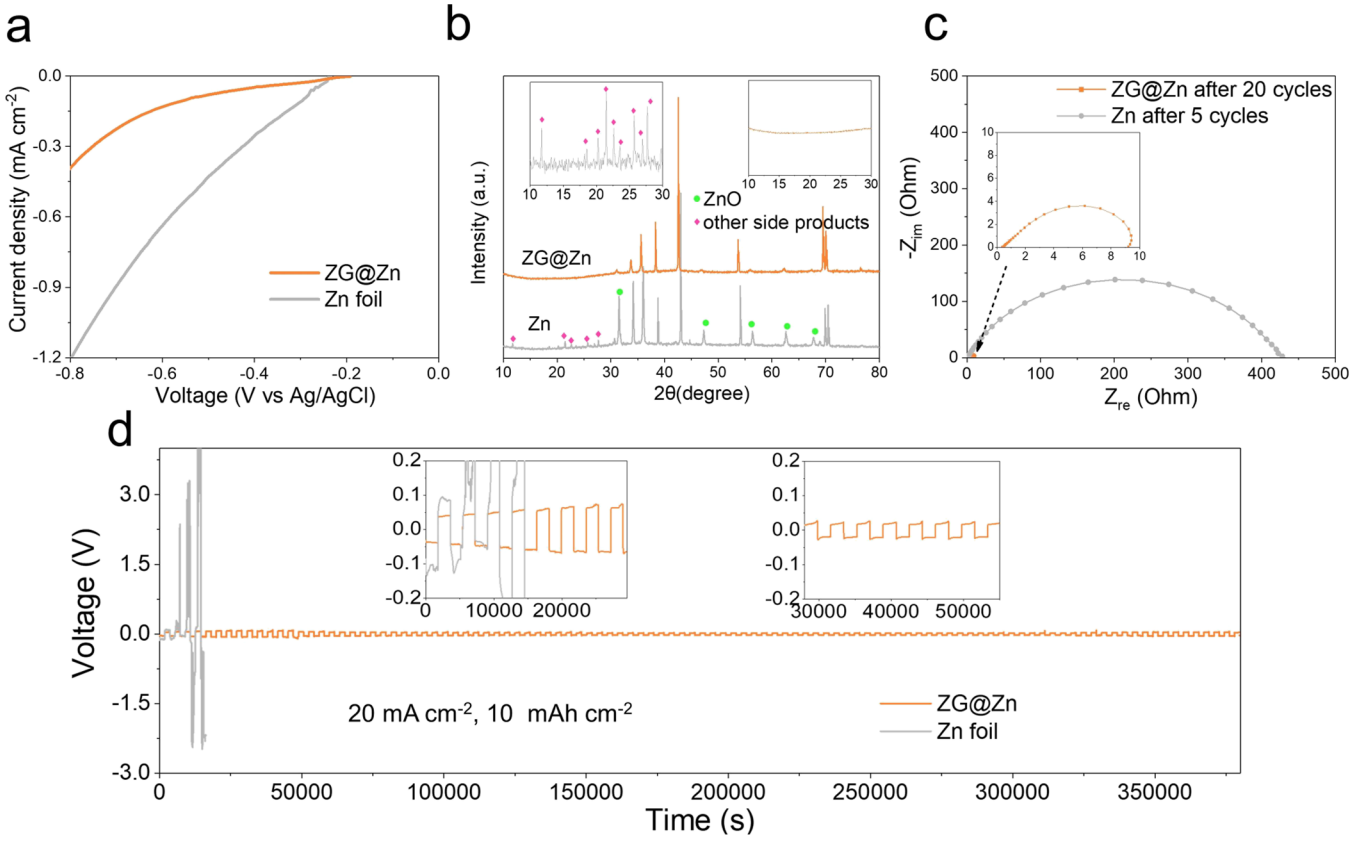

Figure 4. Electrochemical properties of the ZG@Zn anode. (a) Current density versus potential scan for Zn and ZG@Zn electrodes in alkaline media illustrating the effect of the zwitterionic polymer on the HER current. (b) XRD analysis of Zn and ZG@Zn anodes harvested from cells after 10 cycles. (c) Impedance spectra illustrating the dramatic lowering of interfacial resistance after cycling enabled by the zwitterionic polymer gradient interphase. (d) Deep galvanostatic cycling of Zn and ZG@Zn in a 6 M KOH, 0.2 M ZnO electrolyte at a current density of 20-mA cm^{-2} and a capacity of 10 mAh cm^{-2}.

the suppression of electrochemical HER at the SPI. XRD also shows that a variety of side products (i.e., ZnO, $Zn(OH)_2$, etc.) were found after cycling on the uncoated zinc foil (Figure 4b) and that the side-product signal decreased on the ZG interphase (Figure 4b). The morphology after cycling shows the stable interphase for the ZG@Zn anode (Figure S9). Furthermore, FTIR of ZG@Zn before and after cycling both presented a clear peak at 1037 cm^{-1} that came from the SO_3^- group, proving the stability of the ZG interphase during the cycling process in alkaline electrolyte (Figure S10). In addition, electrochemical impedance spectroscopy was performed to understand the interfacial ion transportation processes. The interfacial resistance of symmetric cells (ZG@Zn||ZG@Zn) before cycling refers to the ion diffusion resistance from the PEI to the SPI. Here, the low interfacial resistance ($10 \pm 4\ \Omega$) of the ZG interphase (Figure S11), which is close to the interfacial resistance of an uncoated Zn anode ($8 \pm 5\ \Omega$), indicates excellent ion transportation. Moreover, we measured the interfacial resistance of symmetric cells after cycling to assess side-product accumulation and the interphase stability of the anode (Figure 4c). For an uncoated Zn foil, the interfacial resistance increased from $8 \pm 5\ \Omega$ to $230 \pm 10\ \Omega$ after 5 cycles, indicating side-product accumulation from chemical and electrochemical processes (Figure S11). In stark contrast, the interfacial resistance was constant after 20 cycles with the ZG interphases (from $10 \pm 4\ \Omega$ to $11 \pm 5\ \Omega$) (Figure S11). The stable interfacial impedance after cycling proves the suppression of side reactions in the SPI, such as HER, as well as the electrochemical and mechanical stability of the ZG interphase. Taken together, the ZG interphase exhibited excellent and stable protection against chemical and electrochemical corrosion in a strongly alkaline aqueous environment, which lays the foundation for the reversible cycling of the anode under these conditions.

Zn Anodes and Full Batteries. Figure 4d reports the cycling performance of an uncoated Zn anode and ZG@Zn anode. The reversibility of the anode was investigated in a symmetric cell in 6 M KOH + 0.2 M ZnO electrolyte. A high current density of 20 mA cm^{-2} and an areal capacity of 10 mAh cm^{-2} were applied to evaluate the reversibility. Using the uncoated Zn foil, the Zn symmetric coin cell quickly failed as a result of the serious HER in the alkaline electrolyte, accompanied by severe and quick deformation of the coin cell case due to the gas production. We also observed a large overpotential of 2 V after 3 cycles due to the accumulation of side products and the cell deformation. Notably, highly reversible Zn deposition and stripping were observed with the ZG interphase. Figure 4d shows the reversible electrodeposition of the ZG@Zn anode for a long cycling of ~120 h. The stable and low overpotential (~0.05 V) indicates the effectiveness of the ZG@Zn anode, which could enable a reversible aqueous battery in an alkaline electrolyte. Moreover, ZG@Zn shows stable rate performance at different current densities ranging from 2 to 20 mA cm^{-2} (Figure S12). However, the pristine Zn anode and CZ@Zn presented an unstable overpotential profile at high current density (over 8

https://doi.org/10.1021/jacs.2c06757
J. Am. Chem. Soc. 2022, 144, 19344−19352

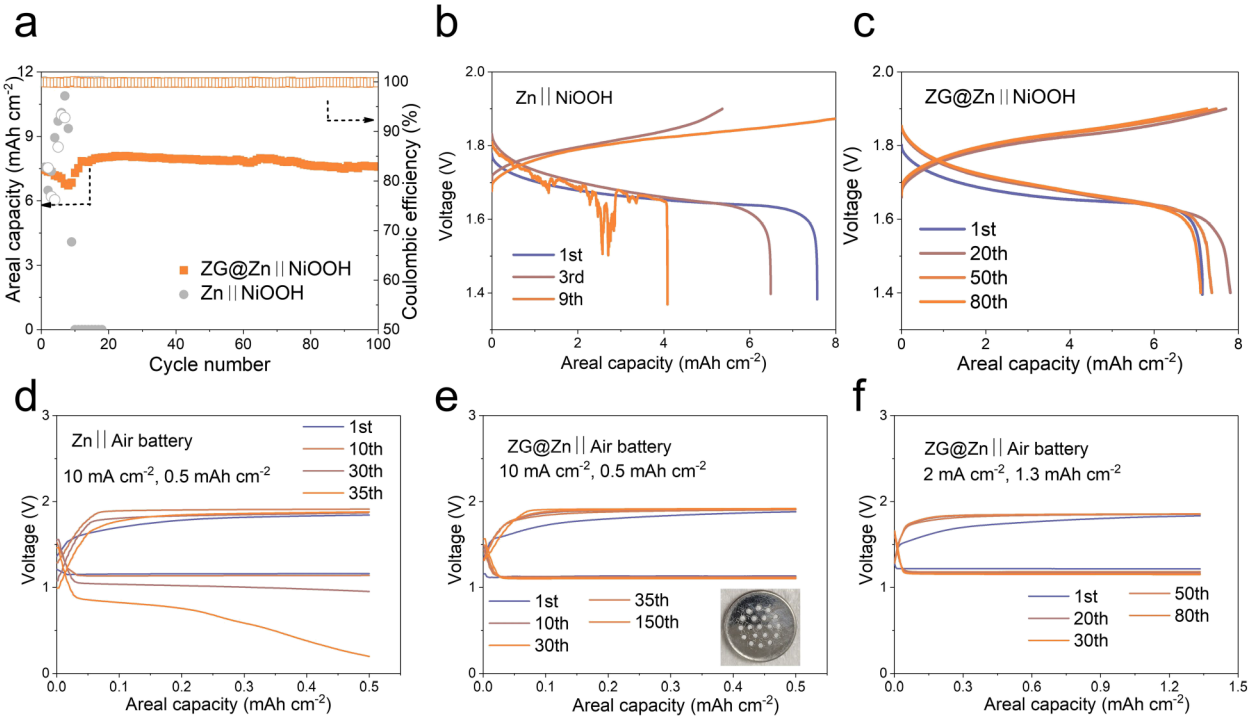

Figure 5. Electrochemical cycling of Zn||NiOOH and Zn||air cells using either Zn or ZG@Zn as the anode. (a) Discharge capacity (left) and Coulombic efficiency (right) of Zn||NiOOH and ZG@Zn||NiOOH batteries cycled at a current density of 10 mA cm^{-2}. The areal capacity was calculated based on the cathode side. (b,c) Voltage−capacity profiles for Zn||NiOOH and ZG@Zn||NiOOH cells at different cycles and at a current density of 10 mA cm^{-2}. (d) Voltage-areal capacity profiles for Zn||air batteries as a function of cycle number. (e,f) Voltage-areal capacity profiles for ZG@Zn||air batteries at 10 mA cm^{-2}, 0.5 mAh cm^{-2} and 2 mA cm^{-2}, 1.3 mAh cm^{-2}, respectively. The inset shows a photograph of the porous cap employed for the Zn||air coin cells.

mA cm^{-2}) and NG@Zn quickly failed at a low current density of 2 mA cm^{-2} (Figure S12).

We used Zn||NiOOH and Zn−air to demonstrate an intercalation battery system and an air battery system. For uncoated Zn foil, Zn||NiOOH full cells quickly failed after 10 cycles due to the irreversible Zn electrodeposition. By using the ZG@Zn anode, Zn||NiOOH full cells can stably run at a high areal capacity of 7 mAh cm^{-2} over 100 cycles (Figure 5a). The voltage−capacity curve at the discharge and charge process proves the stability of the ZG@Zn anode (Figure 5b,c). The stable rate performance of ZG@Zn||NiOOH full cells at different current densities (2−10 mA cm^{-2}) proves the effectiveness of the ZG@Zn anode (Figure S13). Postmortem analysis (SEM and XPS) of Zn and ZG@Zn anodes after cycling in the full cells unveils the protective effect of the ZG interphase. Unlike the coarse ZnO-rich interphase formed in the blank Zn surface (Figure S14), a complete ZG film well protected the Zn anode so that a smooth morphology was observed after cycling in the full cells (Figure S15). XPS results indicated that the surface was well covered by the zwitterionic polymer (Figure S16). On the other hand, the Zn−air battery system also shows obvious differences with and without the protection of the ZG interphase. For uncoated Zn foil, Figure 5d shows that the discharge potential greatly decreases after 35 cycles, indicating a much higher overpotential after cycling, resulting from the accumulation of side products. In contrast, as shown in Figure 5e,f, a ZG interphase extended the cycling performance of Zn−air batteries to 150 cycles and 80 cycles, respectively, at the areal capacities of 0.5 and 1.3 mAh cm^{-2}. Significantly, we used a strict testing environment for the Zn−air batteries here—using the coin cell with a small hole at the bottom and testing in the atmosphere environment (inset in Figure 5e).

CONCLUSIONS

In summary, we achieved reversible Zn electrodeposition in an alkaline aqueous electrolyte using a molecularly designed and vapor deposited zwitterionic gradient (ZG) polymer interphase. The compositional gradient is achieved facilely via a diffusion-limited derivatization reaction and enables effective suppression of the chemical and electrochemical HER processes at the Zn anode. The molecular mechanisms of the suppressed HER and surface passivation reactions were unraveled systematically using experimental and computational demonstrations, which revealed that control of the distribution and activity of water molecules at the electrolyte−anode interface provides a powerful mechanism for lowering their propensity to participate in HER. Consequently, high-performance Zn||NiOOH and Zn||air batteries developed using the ZG interphase strategy show the potential to manifest stable long-term electrochemical performance. This interphase design strategy employed here is straightforward and the concept is in principle readily adaptable in both aqueous and non-aqueous batteries based on any of the other metals of contemporary interest for low-cost and long-duration storage of electrical energy.

ASSOCIATED CONTENT

Supporting Information

The Supporting Information is available free of charge at https://pubs.acs.org/doi/10.1021/jacs.2c06757.

https://doi.org/10.1021/jacs.2c06757
J. Am. Chem. Soc. 2022, 144, 19344−19352

Additional experimental details, materials characterization, and electrochemical analysis (PDF)

AUTHOR INFORMATION

Corresponding Authors

Yong Lak Joo − *Robert Frederick Smith School of Chemical and Biomolecular Engineering, Cornell University, Ithaca, New York 14853, United States;* orcid.org/0000-0002-4646-1625; Email: ylj2@cornell.edu

Rong Yang − *Robert Frederick Smith School of Chemical and Biomolecular Engineering, Cornell University, Ithaca, New York 14853, United States;* orcid.org/0000-0001-6427-026X; Email: ryang@cornell.edu

Lynden A. Archer − *Robert Frederick Smith School of Chemical and Biomolecular Engineering, Cornell University, Ithaca, New York 14853, United States;* orcid.org/0000-0001-9032-2772; Email: laa25@cornell.edu

Authors

Shuo Jin − *Robert Frederick Smith School of Chemical and Biomolecular Engineering, Cornell University, Ithaca, New York 14853, United States;* orcid.org/0000-0003-0425-9143

Peng-Yu Chen − *Robert Frederick Smith School of Chemical and Biomolecular Engineering, Cornell University, Ithaca, New York 14853, United States*

Yufeng Qiu − *Robert Frederick Smith School of Chemical and Biomolecular Engineering, Cornell University, Ithaca, New York 14853, United States*

Zheyuan Zhang − *Robert Frederick Smith School of Chemical and Biomolecular Engineering, Cornell University, Ithaca, New York 14853, United States*

Shifeng Hong − *Department of Materials Science and Engineering, Cornell University, Ithaca, New York 14853, United States*

Complete contact information is available at: https://pubs.acs.org/10.1021/jacs.2c06757

Author Contributions

#S.J. and P.-Y.C. contributed equally to this work.

Notes

The authors declare no competing financial interest.

ACKNOWLEDGMENTS

This work was supported as part of the Center for Mesoscale Transport Properties, an Energy Frontier Research Center supported by the U.S. Department of Energy, Office of Science, Basic Energy Sciences, under award #DE-SC0012673. Support from the Department of the Navy, Office of Naval Research, under ONR award N00014-20-1-2418 is also acknowledged. Y.Q. and Y.L.J. used the Extreme Science and Engineering Discovery Environment (XSEDE), which is supported by National Science Foundation (grant number ACI-1548562). This work made use of the Cornell Center for Materials Research Shared Facilities which are supported through the NSF MRSEC program (DMR-1719875).

REFERENCES

(1) Zheng, J.; Archer, L. A. Controlling electrochemical growth of metallic zinc electrodes: Toward affordable rechargeable energy storage systems. *Sci. Adv.* **2021**, *7*, No. eabe0219.

(2) Chao, D.; et al. Roadmap for advanced aqueous batteries: From design of materials to applications. *Sci. Adv.* **2020**, *6*, No. eaba4098.

(3) Li, Y.; Dai, H. Recent advances in zinc-air batteries. *Chem. Soc. Rev.* **2014**, *43*, 5257−5275.

(4) Zheng, J.; et al. Regulating electrodeposition morphology in high-capacity aluminium and zinc battery anodes using interfacial metal−substrate bonding. *Nat. Energy* **2021**, *6*, 398−406.

(5) Cho, J.; et al. Hydroxyl Conducting Hydrogels Enable Low-Maintenance Commercially Sized Rechargeable Zn−MnO_2 Batteries for Use in Solar Microgrids. *Polymer* **2022**, *14*, 417.

(6) Zheng, J.; et al. Spontaneous and field-induced crystallographic reorientation of metal electrodeposits at battery anodes. *Sci. Adv.* **2020**, *6*, No. eabb1122.

(7) Zheng, J.; et al. Physical Orphaning versus Chemical Instability: Is Dendritic Electrodeposition of Li Fatal? *ACS Energy Lett.* **2019**, *4*, 1349−1355.

(8) Huang, Z.; Choudhury, S.; Gong, H.; Cui, Y.; Bao, Z. A Cation-Tethered Flowable Polymeric Interface for Enabling Stable Deposition of Metallic Lithium. *J. Am. Chem. Soc.* **2020**, *142*, 21393−21403.

(9) Lopez, J.; et al. Effects of Polymer Coatings on Electrodeposited Lithium Metal. *J. Am. Chem. Soc.* **2018**, *140*, 11735−11744.

(10) Parker, J. F.; et al. Rechargeable nickel−3D zinc batteries: An energy-dense, safer alternative to lithium-ion. *Science* **2017**, *356*, 415−418.

(11) Yadav, G. G.; et al. Going beyond Intercalation Capacity of Aqueous Batteries by Exploiting Conversion Reactions of Mn and Zn electrodes for Energy-Dense Applications. *Adv. Energy Mater.* **2019**, *9*, No. 1902270.

(12) Yadav, G. G.; Turney, D.; Huang, J.; Wei, X.; Banerjee, S. Breaking the 2 V Barrier in Aqueous Zinc Chemistry: Creating 2.45 and 2.8 V MnO_2−Zn Aqueous Batteries. *ACS Energy Lett.* **2019**, *4*, 2144−2146.

(13) Yadav, G. G.; et al. Rapid electrochemical synthesis of δ-MnO_2 from γ-MnO_2 and unleashing its performance as an energy dense electrode. *Mater. Today Energy* **2017**, *6*, 198−210.

(14) Liu, M. B.; Cook, G. M.; Yao, N. P. Passivation of zinc anodes in KOH electrolytes. *J. Electrochem. Soc.* **1981**, *128*, 1663.

(15) Wei, X.; et al. Impact of anode substrates on electrodeposited zinc over cycling in zinc-anode rechargeable alkaline batteries. *Electrochim. Acta* **2016**, *212*, 603−613.

(16) Yi, J.; et al. Challenges, mitigation strategies and perspectives in development of zinc-electrode materials and fabrication for rechargeable zinc−air batteries. *Energy Environ. Sci.* **2018**, *11*, 3075−3095.

(17) Wu, Y.; et al. Ion-Sieving Carbon Nanoshells for Deeply Rechargeable Zn-Based Aqueous Batteries. *Adv. Energy Mater.* **2018**, *8*, No. 1802470.

(18) Zhang, Y.; et al. Sealing ZnO nanorods for deeply rechargeable high-energy aqueous battery anodes. *Nano Energy* **2018**, *53*, 666−674.

(19) Cao, L.; et al. Fluorinated interphase enables reversible aqueous zinc battery chemistries. *Nat. Nanotechnol.* **2021**, *16*, 902−910.

(20) Jin, S.; et al. Stabilizing Zinc Electrodeposition in a Battery Anode by Controlling Crystal Growth. *Small* **2021**, *17*, No. e2101798.

(21) Stalin, S.; et al. Ultrathin zwitterionic polymeric interphases for stable lithium metal anodes. *Matter* **2021**, *4*, 3753−3773.

(22) Liu, K.; et al. Lithium Metal Anodes with an Adaptive "Solid-Liquid" Interfacial Protective Layer. *J. Am. Chem. Soc.* **2017**, *139*, 4815−4820.

(23) Yang, C.; et al. Copper-coordinated cellulose ion conductors for solid-state batteries. *Nature* **2021**, *598*, 590−596.

(24) Schlücker, S.; Singh, R. K.; Asthana, B. P.; Popp, J.; Kiefer, W. Hydrogen-bonded pyridine− water complexes studied by density functional theory and Raman spectroscopy. *J. Phys. Chem. A* **2001**, *105*, 9983−9989.

(25) Pápai, I.; Jancsó, G. Hydrogen bonding in methyl-substituted pyridine−water complexes: A theoretical study. *J. Phys. Chem. A* **2000**, *104*, 2132−2137.

(26) Kitano, H.; et al. Structure of water incorporated in sulfobetaine polymer films as studied by ATR-FTIR. *Macromol. Biosci.* **2005**, *5*, 314−321.
(27) Schlenoff, J. B. Zwitteration: coating surfaces with zwitterionic functionality to reduce nonspecific adsorption. *Langmuir* **2014**, *30*, 9625−9636.
(28) Chen, P.; et al. An imidazolium-based zwitterionic polymer for antiviral and antibacterial dual functional coatings. *Sci. Adv.* **2022**, *8*, No. eabl8812.
(29) Chen, P.; Lang, J.; Franklin, T.; Zichen, Y.; Yang, R. Reduced Biofilm Formation at the Air−Liquid−Solid Interface via Introduction of Surfactants. *ACS Biomater. Sci. Eng.* **2021**, No. 0c01691.
(30) Yang, R.; Gleason, K. K. Ultrathin antifouling coatings with stable surface zwitterionic functionality by initiated chemical vapor deposition (iCVD). *Langmuir* **2012**, *28*, 12266−12274.
(31) Erfani, A.; Seaberg, J.; Aichele, C. P.; Ramsey, J. D. Interactions between Biomolecules and Zwitterionic Moieties: A Review. *Biomacromolecules* **2020**, *21*, 2557−2573.
(32) Schmidt, D. A.; Miki, K. Structural correlations in liquid water: A new interpretation of IR spectroscopy. *J. Phys. Chem. A* **2007**, *111*, 10119−10122.
(33) Wallace, V. M.; Dhumal, N. R.; Zehentbauer, F. M.; Kim, H. J.; Kiefer, J. Revisiting the Aqueous Solutions of Dimethyl Sulfoxide by Spectroscopy in the Mid- and Near-Infrared: Experiments and Car-Parrinello Simulations. *J. Phys. Chem. B* **2015**, *119*, 14780−14789.
(34) Jin, S.; et al. Production of fast-charge Zn-based aqueous batteries via interfacial adsorption of ion-oligomer complexes. *Nat. Commun.* **2022**, *13*, 2283.

https://doi.org/10.1021/jacs.2c06757
J. Am. Chem. Soc. 2022, 144, 19344−19352